Highlights

Automatic Tractography and Segmentation using Finsler Geometry based on Higher-order Tensor Fields

Avinash Bansal,Sumit Kaushik,Temesgen Bihonegn,Jan Slovák

- Inversion of Higher-Order Diffusion Tensor
- Tractography Under Finsler Setting
- Segmentation via Finsler Tractography

Automatic Tractography and Segmentation using Finsler Geometry based on Higher-order Tensor Fields

Avinash Bansal[a], Sumit Kaushik[b], Temesgen Bihonegn[a] and Jan Slovák[a,*]

[a]Department of Mathematics and Statistics, Faculty of Science, Kotlářská 2, 611 37, Brno, Czech Republic
[b]Department of Radiology and Nuclear Medicine, St. Olav's University Hospital, Torgarden N0-7006, 3250, Trondheim, Norway

ARTICLE INFO

Keywords:
HARDI
Tractography
Segmentation
HOT inversion
Finsler geometry
White matter structure

ABSTRACT

We focus on three-dimensional higher-order tensorial (HOT) images using Finsler geometry. In biomedical image analysis, these images are widely used and depend on the diffusion profiles inside the voxels. The diffusion information is stored in the so-called diffusion tensor (D). Here, our study concentrates on its application to brain white matter. Our goal is to reveal the architecture of neural fibers and image segmentation to analyze brain structure. To deal with the construction of the underlying fibers, the inverse of the second-order diffusion tensor (D), understood as the metric tensor (D^{-1}), is commonly used. It is challenging to find an analogue of such an inverse in the HOT case. In the case of complex diffusion profiles, neither the Finsler norm Astola and Florack (2011) nor the streamline tractography method properly track the fibers. To enable efficient computation, we propose a brand-new approach to the inversion of a diffusion HOT and an optimal way of fiber tracking in the Finsler setting. Thus, we can handle complex structures with high curvatures and crossings, even in the presence of noise. Based on our novel tractography approach, we also introduce a new segmentation method. We feed the detected fibers as the initial position of the contour surfaces to segment the image using the relevant active contour method (i.e., initiating the segmentation from inside the structures). This feature makes it more robust and faster, and allows us to distinguish individual objects in complex structures, even under noise.

1. Introduction

Diffusion Weighted Imaging (DWI) is a non-invasive technique widely used in medical images to measure the diffusion characteristics of water molecules, which gives the direction and magnitude of diffusion. In diffusion tensor imaging (DTI) modality, the information on the diffusion at each voxel is stored in a second-order diffusion tensor (D). It can be represented by a symmetric positive definite matrix (SPD) of size 3×3. Due to this property, it lies in the Riemannian symmetric space Basser, Mattiello and LeBihan (1994b); Fletcher, Lu and Joshi (2003); Lenglet, Rousson, Deriche, Faugeras, Lehericy and Ugurbil (2005); Pennec, Fillard and Ayache (2006); Kingsley (2006); Fletcher (2013); Krajsek, Menzel and Scharr (2016). This DTI model reveals the structure of brain white matter. It assumes that there is a maximum of one fiber orientation present at each voxel.

However, it is known that each voxel can contain more than one fiber orientation to reflect the crossing between the fibers in the white matter region. To overcome the limitation of DTI, the higher angular resolution diffusion imaging model (HARDI) is introduced and used to analyze the complex diffusion profile Tuch et al. (2002). It can distinguish between multi-fiber architectures inside a voxel. It has proven its effectiveness in modeling white matter brain structures along with the fiber intersection regions. There are numerous methods to reconstruct the architecture of brain tissue using HARDI data Tournier, Calamante, Gadian and Connelly (2004); Özarslan, Shepherd, Vemuri, Blackband and Mareci (2006); Tournier, Yeh, Calamante, Cho, Connelly and Lin (2008). Each approach provides the orientations of several white-matter tracts inside a voxel. The model assumes that the diffusion profile at each voxel has local maxima corresponding to each dominant direction of the underlying fiber tracts.

The diffusion coefficients $D(\mathfrak{g})$ are computed from the signal $S(\mathfrak{g})$ using the Stejskal-Tanner equation defined as

$$S(\mathfrak{g}) = S(0)\exp(-bD(\mathfrak{g})), \tag{1}$$

*Corresponding author
slovak@muni.cz (J. Slovák)
ORCID(s): 0000-0003-3114-5870 (A. Bansal); 0000-0002-4146-291X (S. Kaushik); 0000-0002-0210-3252 (T. Bihonegn); 0000-0001-8986-1955 (J. Slovák)

where $\mathtt{g}$ is the direction of the gradient, $S(0)$ is the signal obtained in the absence of the direction of the gradient, b is a parameter associated with the diffusion imaging protocol and has units of s/mm^2.

If the diffusion profile of water molecules can be modeled using a Gaussian process, then the equation (1) can be written as

$$S(\mathtt{g}) = S(0)\exp(-b\mathtt{g}^T D\mathtt{g}), \tag{2}$$

i.e., using the DTI modality.

The diffusion process is a physical phenomenon and due to the antipodal symmetry of the gradient directions, the tensors calculated from equation (1) should be positive definite Barmpoutis, Hwang, Howland, Forder and Vemuri (2009); Barmpoutis and Vemuri (2010) and of even order, respectively. For example, the 4th order tensor can be represented by $3\times3\times3\times3$ a multidimensional array, the 6th order tensor can also be represented by $3\times3\times3\times3\times3\times3$ multidimensional array, and so on.

Diffusion data and fiber tractography are the most commonly combined approaches to reconstruct the architecture of brain tissue. The two broadest classes of tractography algorithms are deterministic tractography Mori, Crain, Chacko and Van Zijl (1999); Basser, Pajevic, Pierpaoli, Duda and Aldroubi (2000); Chu, Huang, Sun, Zhang, Liu and Zhu (2015); Bansal, Kaushik, Bihonegn and Slovák (2021) and probabilistic tractography Björnemo, Brun, Kikinis and Westin (2002); Behrens, Woolrich, Jenkinson, Johansen-Berg, Nunes, Clare, Matthews, Brady and Smith (2003); Friman, Farneback and Westin (2006). Deterministic tractography is based primarily on a streamline algorithm, where the local direction of the tract is defined by the principal eigenvector of the diffusion tensor. In the case of probabilistic tractography, it travels through all possible trajectories and provides a simulated distribution of the fiber tract. Many diffusion and tracking orientation data representations have been used to customize tractography algorithms, including DTI, q-ball Tuch et al. (2002), and multiple tensor models.

For fiber tracking, Finsler geometry is used by Melonakos, Pichon, Angenent and Tannenbaum (2008); Astola and Florack (2011); Sepasian, ten Thije Boonkkamp, Florack, Romeny and Vilanova (2014) to deal with the structure of multiple fibers. It is best suited for the multiple diffusion profile. It is more general than Riemannian geometry, since the tangent norms are not necessarily induced by inner products.

To properly handle the fiber architecture via curve-length minimizers, we need a norm on the velocities, which would charge the directions of the principal eigenvectors with low costs, while the orthogonal directions become expensive. In the DTI modality, this is achieved by the metric tensor, which is the inverse of the diffusion profile, or by sharpening the metric tensor. It is treated as a Riemannian metric O'Donnell, Haker and Westin (2002); Hao, Whitaker and Fletcher (2011) and is used to construct white matter tracts as geodesics on the resulting manifold. While in the case of DTI, it is easy to take the inversion, the analogous task for HOT has not been satisfactorily handled yet. In this paper, we suggest bypassing this problem by employing the HOTs defined by the reciprocal values of the signal $S(\mathtt{g})$, or its sharpening.

Segmentation is another crucial aspect of medical image analysis and, in the structure of white matter, plays a vital role in diagnostics. During recent decades, DTI-based and HARDI-based segmentation approaches have been developed to segment brain tissue Hagmann, Jonasson, Deffieux, Meuli, Thiran and Wedeen (2006); Descoteaux and Deriche (2009); de Luis-García, Westin and Alberola-López (2011). It is possible to classify segmentation algorithms into three categories: manual segmentation, segmentation using prior knowledge of images, and segmentation without prior knowledge of images, based on similarities and topological consistency between different individuals in the same tissues Wang, Zhao, Guo, Qi, Fan and Meng (2019).

Many image modalities have been processed and segmented into separate regions based on biases or unbiased contours Mumford and Shah (1989); Malladi, Sethian and Vemuri (1995); Caselles, Kimmel and Sapiro (1997); Sethian (1999); Chan and Vese (2001); Prakash, Zhou, Morgan, Hanley and Nowinski (2012); Kaushik and Slovák (2018, 2019). These techniques have some drawbacks and cannot handle complex images accurately, for example, the donut shape. Here, we fix this problem using tractography data for the initiation of the segmentation.

This paper is organized as follows. Section 2 provides a summary of our contributions. Section 3 contains a short introduction to Finsler geometry. Section 4 defines the geodesic equation in the Finsler setting. Section 5 discusses our state-of-art, i.e., the HOT inversion, fiber tracking approach, and segmentation method in detail with results. In Section 5.1 we introduce the inversion of diffusion HOT. In Section 5.2 we present the intuitive way to use the Finsler approach to track fibers in biomedical images. Section 5.3 describes the tractographic segmentation method. In Section 5.4 we show the 3D image result of Finsler fiber tracking and segmentation on simulated data and on real brain HARDI data. The last section 6 contains conclusions and future scope.

2. Our Contributions

We aim to design effective and efficient tractography and segmentation methods in the Finsler framework to handle multi-fiber and complex structures. We feed the fiber tractography result as the initiation data to segment these structures. We fully automate our method to avoid user interaction. The contributions are summarized in the following.

1. In DTI, a natural way to track fibers is to use the metric tensor D^{-1}. This approach has been exploited in the DTI literature Basser, Mattiello and LeBihan (1994a); Basser et al. (1994b); Fletcher et al. (2003); Lenglet et al. (2005); Pennec et al. (2006); Fletcher (2013); Krajsek et al. (2016). However, in the case of HOT, it is difficult to find an apropriate general analogue for the inverted diffusion tensor. The HARDI data provide much more directional information Tuch et al. (2002), and we may apply the Finsler norms, which can be understood as metrics depending on position and direction. We propose to use the so-called nth root Finsler norms associated with the nth order HOTs, approximating the reciprocal values of the diffusion signal. Another inversion approach based on spherical inversion is introduced in Astola, Sepasian, Haije, Fuster and Florack (2014), but it requires large calculations and does not provide good control over errors. Our procedure preserves distances and inner products (see Fig. 2), and it works for all higher-order diffusion tensors (see Fig. 1). Furthermore, we observe that even in the case of HOT, sharpening of the inverse of the diffusion tensor can be achieved by powering the signal $S(\mathfrak{g})$.

2. In DTI modality, the streamline tractography method is used to handle the single fiber structure but not to deal with multiple fibers (e.g. crossing, merging, kissing fibers, etc.). For the description of multiple fibers, the Finsler norm is better suited because it is a function of both position and direction at a particular point. Melonakos et al. (2008) used a dynamic programming approach to compute optimal curves with respect to a Finsler norm, without computing the Finsler metric tensors and associated eigensystems. However, this method does not handle the complex diffusion profile; for example, subcortical fibers with very high curvature. Subsequently, Astola and Florack (2011) proposed a generalized streamline procedure and Sepasian et al. (2014) proposed a multivalued geodesic approach; for HARDI in the Finsler setting. Both approaches work well, but cannot adequately handle fiber intersection areas at small angles. Here, we use the features of the Finsler norm and the hybrid streamline tractography Bihonegn, Kaushik, Bansal, Vojtíšek and Slovák (2021) in the Finsler setting to handle more complex structures (see Figs. 10 (b) and 11 (b)) and small-angle intersections even under noise (see Figs. 8 and 9). We can track fibers more accurately in white matter structures using this method.

3. For segmentation, we use the unbiased contour method. The contour is free to shrink or expand depending on the features of the image. Similarly to the approach in Kaushik and Slovák (2018, 2019), we use the localized active contour segmentation method. Due to the choice of the initial contour position and contour shape, this approach has some shortcomings when segmenting complex structures (see Figs. 10 (a) and 11 (a)), which we have resolved. We suggest feeding the detected fibers as the initial contour position. Further, we employ the second-order projections of the 4th order tensors under the Finsler framework in the following way. The 2nd order tensor fields used for segmentation are obtained by calculating certain quadratic mean of the direction-dependent metric tensor at individual voxels, and we use spectral-quaternion (SQ) interpolation for the distance approximation, which is more suitable even in the presence of noise Tschumperle and Deriche (2001). This allows us to run the segmentation algorithm directly in 3D, and we get faster and more accurate results even for more complex images (see Fig. 11).

3. Finsler Geometry

In Euclidean geometry, when the medium is homogeneous and isotropic, the shortest paths are straight lines. In simple inhomogeneous cases, the Riemann geometry is suitable and the shortest paths are geodesics induced by the Levi-Civita connection Do Carmo and Flaherty Francis (1992). These connections are a set of rules that define how to take derivatives over the Riemann manifold. Finsler geometry is appropriate for defining the directional structure when the medium is inhomogeneous and anisotropic to a much more general extent. Unlike Riemann geometry, here distances can be understood via a direction-dependent inner product, computed from a position-dependent norm. The Finsler norm can be used to analyze diffusion data in geometric terms when fitting higher-order tensors to the HARDI data. Finslerian approach provides a collection of metric tensors instead of one metric tensor per voxel. If we denote a

symmetric 4th order tensor by T, then using the Einstein summation notation [1]

$$T(x,y) = T_{ijkl}(x)y^i y^j y^k y^l, \tag{3}$$

where x is the spatial coordinate and y is the gradient direction coordinate. The spherical inversion, $\tilde{T}(x,y)$, is given as

$$\tilde{T}(x,y) = \frac{\bar{T}(x)}{T(x,y)} = \tilde{T}_{ijkl}(x)y^i y^j y^k y^l, \tag{4}$$

where y is a unit gradient direction, $\bar{T}(x)$ is the average of the HOT over the unit sphere, i.e.,

$$\bar{T}(x) = \int_{|y|=1} T(x,y)dy, \tag{5}$$

and $\tilde{T}$ is the HOT that fits the inverted diffusion data. Astola and Florack (2011) propose Finsler norm, $F(x,y)$ corresponding to the 4th order tensor can be defined as

$$F(x,y) = (\tilde{T}_{ijkl}(x)y^i y^j y^k y^l)^{1/4}. \tag{6}$$

The nth root Finsler form of any tensor T of order n is

$$F(x,y) = (T_{i_1 i_2 \ldots i_n}(x)y^{i_1} y^{i_2} \ldots . y^{i_n})^{1/n}. \tag{7}$$

This norm satisfies the properties of differentiability, homogeneity, and strong convexity. By major symmetry, the number of independent coefficients for the tensor of order n is reduced from 3^n to $\frac{1}{2}(n+1)(n+2)$. For example, for the 4th order tensor, there are 15 independent coefficients of the total $3^4 = 81$. The direction-dependent metric tensors (for each choice of y) are derived from the Finsler norm as follows

$$g_{ij}(x,y) = \frac{1}{2}\frac{\partial^2 F^2(x,y)}{\partial y^i \partial y^j}. \tag{8}$$

This tensor is strictly positive-definite due to its convex property. If $F(x,y) = \sqrt{g_{ij}(x)y^i y^j}$, then it reduces to the Riemannian metric $g_{ij}(x,y) = g_{ij}(x)$.

4. Finsler Geodesic Equations

A geodesic in the Finsler setting minimizes the length of a curve between two fixed endpoints, as in Riemannian geometry. The Euler-Lagrange equations for the critical points of the variational length functional, provide the differential equations for the minimizers, Shen (2001).

Let M be a smooth n dimensional manifold with local coordinates (x^i). The length $L_F(\chi(t))$ of the smooth curve $\chi : [a,b] \to M$ is defined as

$$L_F(\chi(t)) = \int_a^b F(\chi(t), \dot{\chi}(t))dt. \tag{9}$$

The geodesic equations, i.e., the Euler-Lagrange equations for the equation (9) are

$$\ddot{\chi}^i(t) + 2G^i(\chi(t), \dot{\chi}(t)) = 0, \tag{10}$$

where G^i are called the geodesic coefficients, defined by

$$G^i(x,y) = \frac{1}{4}g^{il}(x,y)\left(\frac{\partial g_{kl}(x,y)}{\partial x^j}y^k y^j + \frac{\partial g_{jl}(x,y)}{\partial x^k}y^j y^k - \frac{\partial g_{jk}(x,y)}{\partial x^l}y^j y^k\right). \tag{11}$$

[1] Einstein notation: whenever two indices with the same labels appear on the same side of an equation, one assumes that there is an implicit sum over those indices.

Formally, an alternative form of these Finslerian equations (10) and (11) can be written as identical to the Riemann geometry, respectively, as

$$\ddot{\chi}^i(t) + \Gamma^i_{jk}\dot{\chi}^j\dot{\chi}^k = 0, \tag{12}$$

and

$$\Gamma^i_{jk}(x,y) = \frac{1}{2}g^{il}(x,y)\left(\frac{\partial g_{kl}(x,y)}{\partial x^j} + \frac{\partial g_{jl}(x,y)}{\partial x^k} - \frac{\partial g_{jk}(x,y)}{\partial x^l}\right), \tag{13}$$

which is the desired form of the equations. Compared to the Riemannian case, here Γ^i_{jk} are functions of both position and direction.

5. Fiber Tracking and Segmentation under Finsler Setting

In diffusion tensor imaging, the Finsler geometry seems to be a perfect tool for understanding heterogeneous and highly anisotropic media. Since the distances are defined via direction-dependent inner products, it is able to model multi-fiber diffusion profiles.

Our aim is to implement a fast and robust 3D segmentation algorithm for the structure of white matter. We suggest initiating our segmentation method by detected fibers, thus starting with a novel approach to tractography first.

In order to choose the initial positions to begin tracking, we select the voxels with fractional anisotropy, $\mathrm{FA}_m(x) \geq 0.7$, (see equation (16)). During the algorithm, these voxels are controlled by a certain flag variable (see Fig. 5). Finally, the fibers collected as the tracking output are fed into an active contour algorithm for segmentation. Our enhanced algorithms produce accurate fiber tracks, and provide fast and accurate segmentation of complex images.

The experiments were carried out on a desktop with an Intel(R) Core(TM) i5-7500T CPU @ 2.70GHz and 16.0GB RAM using MATLAB 2019a. We show the performance of our approach on both synthetic and real data. For this, we use fanDTasia ToolBox Barmpoutis et al. (2009); Barmpoutis and Vemuri (2010)) to produce synthetic images that closely mimic the diffusion of water in white matter fibers. We used $b = 1500s/mm^2$ and two sets of different gradient directions (81 for synthetic data and 64 for real data).

5.1. Inversion of Higher Order Diffusion Tensor

From a technical point of view, the signal phase in diffusion magnetic resonance imaging (MRI) is so heavily corrupted that it is not informative due to noise and artifacts. Therefore, practical implementations limit this generalization to the estimation of even-order tensors of signal magnitude Liu, Mang and Moseley (2010); Schultz, Fuster, Ghosh, Deriche, Florack and Lim (2014). In that sense, a diffusion tensor should be an even-order fully symmetric tensor. In DTI mode, the inverse of the diffusion tensor (D) is a metric tensor (D^{-1}) that lies in the Riemann space used to reveal the architecture of the underlying fibers O'Donnell et al. (2002). The diffusion tensor values along the directions in $\mathbb{R}^3$ tell how far a particle can diffuse in a given time (having units of s/mm^2 corresponding to acceleration). For tractography, we would like to consider a metric tensor which charges the directions with the greatest acceleration least, while those with the smallest acceleration would be charged most. Thus, the inverse D^{-1} seems to be the perfect choice to start with.

In DTI, inversion of the diffusion tensor is easy. In HARDI, we cannot take the inverse directly from the matrix representations of the 4th order tensors. Proper inversion is required to preserve specific properties, such as the distance and angle near each point on a surface. However, by using specific representations, we can do this to some extent. Vuorinen (2006) presents Möbius-inverse of diffusion HOT, which is typically not a spherical tensor. There is another better approach to invert the HOT diffusion based on spherical inversion Astola et al. (2014), but it requires large computations. We propose a simple and efficient way to define the right "inverted" diffusion HOT based on the inversion of the signal. This inversion behaves well in terms of the inner product and distances (see Fig. 2).

Equation (1) reflects the reduction in the signal due to the application of a pulsed gradient, and they ensure that the change will be proportional to the amount of diffusion. Our strategy is based on the inversion of this signal. As a result, if we invert the signal $S(\mathrm{g})$ at the initial stage, that is, $S_{new}(\mathrm{g}) = \frac{1}{S(\mathrm{g})}$, then we get the following equation

$$S_{new}(\mathrm{g}) = S(0)\exp(-b\tilde{D}(\mathrm{g})), \tag{14}$$

where the computed diffusion profile $\tilde{D}(\mathrm{g})$ represents the inverse of the diffusion tensor.

In the DTI modality, this approach provides yet another numerical way to obtain the approximation of the inverse tensor D^{-1}, used in the fiber tracking. Intuitively, we want to charge the directions with fast diffusion very little and vice versa. Thus, our formula (14) provides the proper analogue of the inverted tensor directly, in general.

Furthermore, for fiber tracking, the sharpening strategy improves the tracking result. Sharpening has been performed by powering the tensor in the DTI modality case and is well defined in Descoteaux, Lenglet and Deriche (2007); Dela Haije, Sepasian, Fuster and Florack (2016); Bihonegn et al. (2021). Here, we observe that the sharpening of the metric tensor can also be achieved by powering the initial signal, $S(\mathfrak{g})$. For example, in equation (14) replacing $S_{new}(\mathfrak{g})$ by $S_{sharp}(\mathfrak{g})$ where $S_{sharp}(\mathfrak{g}) = \frac{1}{S(\mathfrak{g})^2}$ and after solving it, the diffusion profile ($\tilde{D}(\mathfrak{g})$) gives the sharpened metric tensor. This can be extended for HOT to obtain the sharpened inverted diffusion tensor.

Fig. 1 illustrates the tensors of various orders and their inverted versions by their glyphs. We performed an experiment to ensure that the inverted tensor retains specific properties. For each instance, we randomly took two diffusion tensors of the 4th order and calculated the distance defined in Barmpoutis et al. (2009) between these two diffusion tensors and the distance between their inverted tensors and plotted their graph. Similarly, we perform the same operation for the inner product between them. Fig. 2 shows the stability of our inversion method; in both cases, the inverse of the diffusion tensor has a pattern similar to that of the diffusion tensor.

A symmetric positive definite tensor of 4th order in three dimensions can also be represented by an SPD tensor of 2nd order in six dimensions. Therefore, the Riemannian metric of the space of 6×6 SPD matrices can be used for SPD 4th order tensor computations Barmpoutis et al. (2009). The six-dimensional SPD tensors obtained in Ghosh, Papadopoulo and Deriche (2012); Gur and Johnson (2014) are more preferable and can be expressed in the Voigts notation as a matrix of size 6×6 Brannon (2018). Fig. 3 clearly illustrates that the spherical inversion tensor Astola et al. (2014) and the inversion of the Voigt matrix (i.e., the Voigt inversion tensor) do not retain the distance properties. This is because in both cases, the 4th order tensor is represented by the 2nd order tensor using the 9×9 or 6×6 matrix that lies in the semi-Riemann or Riemann space. These representations of the HOT might lead to failures in subsequent processing.

Fig. 4 indicates the 4th order diffusion tensor field and its inverted diffusion tensor field of the corpus callosum, which is a part of the real brain image.

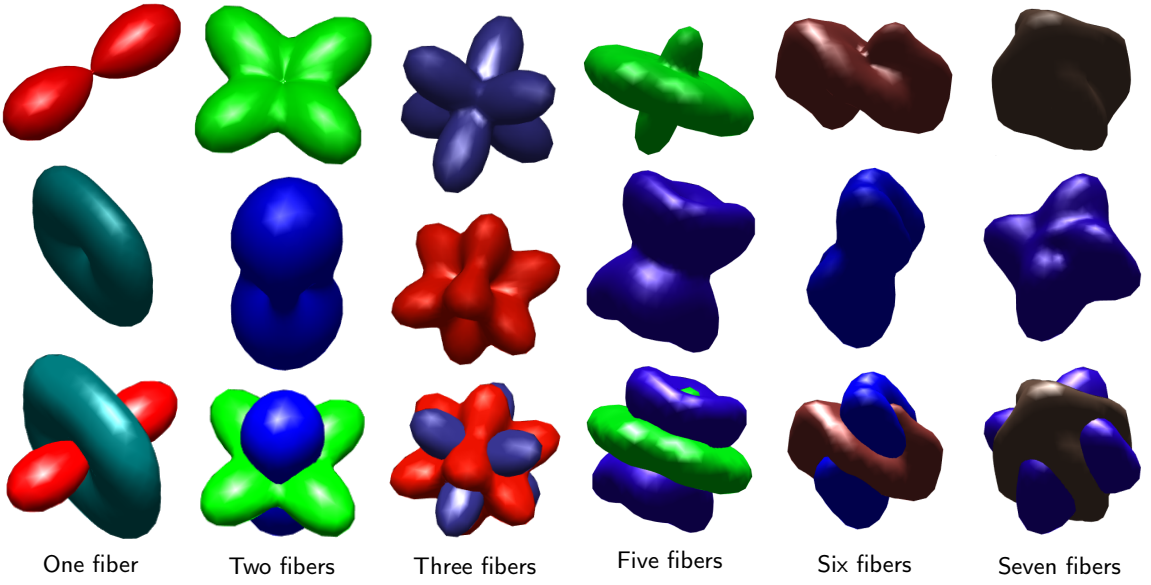

Fig. 1: Tensor glyphs of the orders 4, 6, and 8. The rows show the diffusion tensors, their inverted versions, and the combined behavior of the diffusion tensors and the inverse tensors, from top to bottom, corresponding to each other. 4th order tensors appear in the first two columns, 6th order tensors appear in the third and fourth columns, while the last two columns show the 8th order tensors. The number of fibers per voxel is indicated in the bottom line.

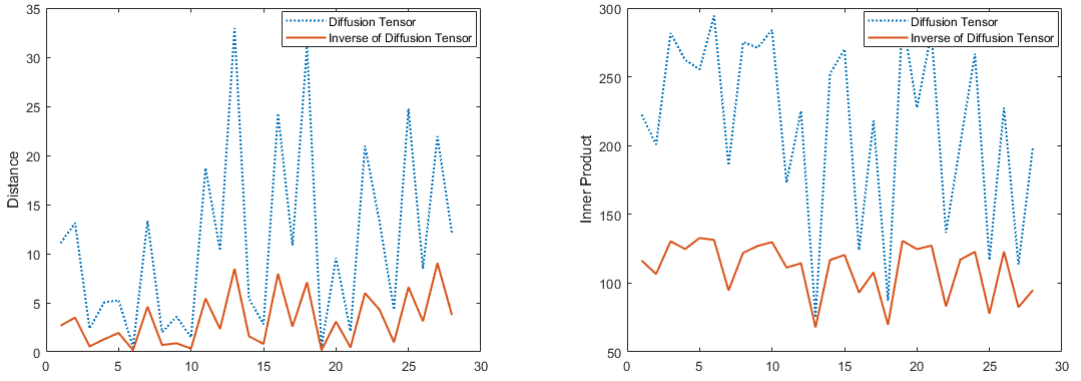

(a) Distance (b) Inner Product

Fig. 2: These graphs show that inverted HOT preserves distance and inner product properties. Graph a) x-axis indicates the individual instances of randomly chosen diffusion tensors and their computed inverses by our inversion method. Along the y-axis, the dotted line shows the distance between diffusion tensors and the solid line shows the distance between inverse of diffusion tensors. Similarly, graph b) shows the inner products between them.

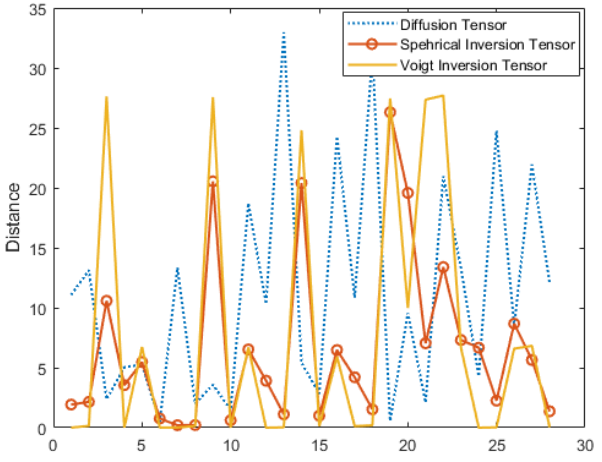

Fig. 3: The spherical inversion tensor Astola et al. (2014) and the inversion of the Voigt diffusion notation (i.e. Voigt inversion tensor) fail to retain the distance (similar to Fig. 2 (a)) properties. While the diffusion tensor is shown in its proper scale, the two other inversions of diffusion tensors are scaled down by a multiplicative factor.

5.2. Fiber Tracking in HARDI using Finsler Approach

In the DTI streamline mode, there is a direct approach to track the fiber following the principal direction of the diffusion tensor. This method cannot address the problems of fiber crossing, merging, and kissing. In the Finsler setting, we have multiple metric tensors for each position. In the HOT case, the Finsler norm defined in Melonakos et al. (2008) can deal with the above-mentioned problems to some extent, but cannot deal with fibers having high curvature, such as subcortical fibers. Another straightforward approach under the Finslerian framework is the generalization of DTI Astola, Jalba, Balmashnova and Florack (2011) which solves the problem of high curvature. Subsequently, on the basis of Finsler geometry, Sepasian et al. (2014) proposed a multi-valued numerical solution of the geodesic equation. They captured all geodesics that arrive at a single voxel instead of computing the shortest one. The approaches mentioned above still show some shortcomings for small-angle fiber intersection regions. Our approach uses the features of both

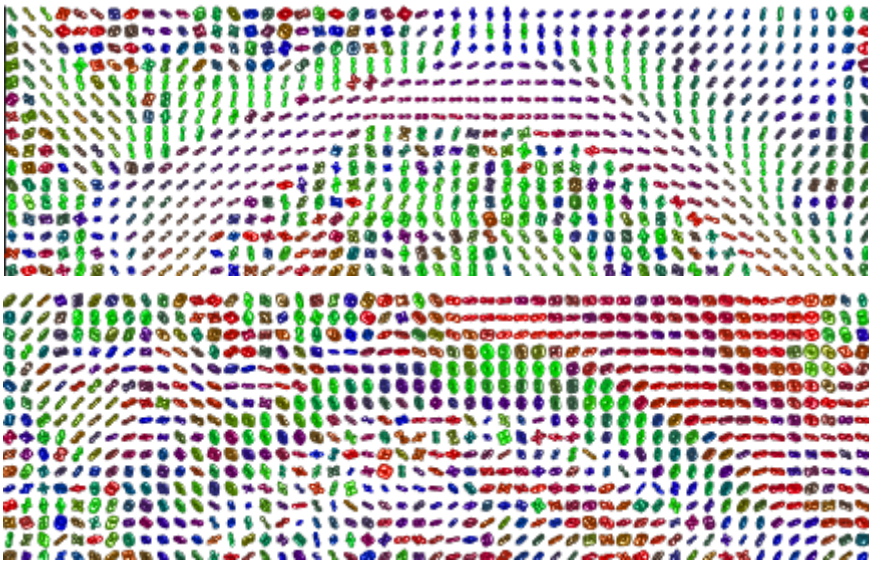

Fig. 4: 4th order diffusion tensor field (top image) and its inverted diffusion tensor field (bottom image) of the corpus callosum, which is a part of the real brain image.

the Finsler norm and the hybrid streamline. It works well to handle high-curvature and small-angle intersecting fibers, even in the presence of noise.

From the equation (8), we know that $g_{ij}(x, y)$ has SPD properties, so the mean of all SPDs at x, denoted as $m_{ij}(x)$ is also an SPD matrix. It is defined as follows

$$m_{ij}(x) = \frac{1}{w} \sum_{s=1}^{w} g_{ij}(x, \mathbf{y}_s), \tag{15}$$

where $\mathbf{y}_s$ represents the sth gradient direction and w represents the number of gradient directions that lie on a unit hemisphere at position x. To begin tracking in the tractography algorithm, we need seed points. To make our algorithm fully automatic, we use the fractional anisotropy $\mathrm{FA}_m(x)$, which is represented as

$$\mathrm{FA}_m(x) = \mathrm{FA}\left(\tilde{m}_{ij}(x)\right), \tag{16}$$

where $\tilde{m}_{ij}(x)$ is the inverse of $m_{ij}(x)$ and FA is the fractional anisotropy[2]; therefore, $\mathrm{FA}_m(x)$ is in $[0, 1]$. These values are related to the probability that the voxels are anisotropic, a high value suggests that only one fiber will be present, and a low value suggests that there will be an isotropic voxel. Therefore, we choose $\mathrm{FA}_m(x) \geq 0.7$ for the seed points. In the tractography algorithm, we need to calculate the angle between two directions (we always consider the smaller one of the two possibilities).

In our discretized approach to direction-dependent metrics, for every position, we have multiple 2nd order tensors, one for each direction. Fig. 6 a) shows the glyph of a 4th order tensor, while Fig. 6 b) illustrates the bunch of the relevant tensors of 2nd order. To reduce computational time and make our algorithm more effective, we choose the 30 tensors of w with the highest maximal eigenvalues. Each pair of these tensors displays the angle between the directions of their principal eigenvectors. As an observation in the case of a single fiber per voxel, the maximum angle (max_an) of the angles of these pairs is 22°. For this reason, in our experiment, we choose the threshold angle value (th_an) 25° to decide the intersection of the fibers. We choose this threshold angle parameter for its stability in high noise, compared to other possibilities (e.g., FA values).

To employ the features of both the Finsler norm and hybrid streamline, the image is broadly divided into two categories, non-intersecting (one fiber per voxel) and intersecting (two or more fibers per voxel) regions. In Fig. 7

[2] $\mathrm{FA} = \sqrt{\frac{1}{2}} \frac{\sqrt{(\lambda_1-\lambda_2)^2+(\lambda_2-\lambda_3)^2+(\lambda_3-\lambda_1)^2}}{\sqrt{\lambda_1^2+\lambda_2^2+\lambda_3^2}}$, where $\lambda_1, \lambda_2, \lambda_3$ are eigenvalues of that tensor corresponding to eigenvectors.

rectangular boxes of cyan and yellow color represent the non-intersecting and intersecting regions, respectively. In the case of non-intersecting regions, we follow the hybrid streamline method by choosing the metric tensor $m_{ij}(x)$. In the case of intersecting regions, we follow the Finsler norm by choosing the optimal direction-dependent metric (as explained below), out of those thirty metrics.

In the case of non-intersecting regions, the initial position and the initial direction (i.e., principal direction of $\tilde{m}_{ij}(x)$) feed to the ordinary differential equation (ODE) solver. Then, using the Riemannian geodesic equation (5) in Bihonegn et al. (2021), we get the next position and direction. Keep the position the same; the direction is replaced by the principal eigen direction (PE) of $\tilde{m}_{ij}(x)$. We choose the metric $m_{ij}(x)$ because it is much more stable than the other metrics, even in the presence of noise.

In the case of intersecting regions: during tracking, we always keep records of our previous position and PE. To resolve the voxel at the current position, we first compute the angles (i.e., $\binom{30}{2}$) angles between all pairs of PE of the direction-dependent 30 diffusion tensors. Second, we find the maximum angle of those and compare it with the threshold angle. If the maximum angle is greater than the threshold angle, then we declare the voxel to be the intersection. To choose the minimum possible deviation in the tractography path compared to the previous position, we computed the angles between the previous direction and the PE of the current position of the 30 diffusion tensors representing the Finsler norm. We choose the metric in which PE has a minimum angle with the previous direction. Then we feed the position and direction of the gradient of the corresponding direction-dependent metric to the ODE solver, and by equation (12), we get the next position and direction.

Integration of geodesics continues until one of the stopping criteria (as explained below) is reached. We can accurately track the fiber in complex fiber structures, even under high noise. To cover the full image, the tracking takes place in both opposite directions of PE for every initial position.

Activation functions have been used in tractography, Fuster et al. (2016); Bihonegn et al. (2021), to scale the metric tensors and improve the performance. In our algorithm, we use the ratio of the maximum and minimum eigenvalues λ_{max} and λ_{min} and we rescale the metric tensor as $\bar{g}_{ij}(x,y) = g_{ij}(x,y)\frac{\lambda_{max}}{\lambda_{min}}$, or $\bar{m}_{ij}(x) = m_{ij}(x)\frac{\lambda_{max}}{\lambda_{min}}$, in order to give bigger weight to the anisotropic voxels in the interpolations. Our approach to the inversion of the diffusion tensor has provided very satisfactory results, so we did not further experiment with sharpening in this work.

To maintain the stability and smoothness of the path, we use trilinear interpolation of the metric tensors of the neighboring voxels on a finer grid. In 3D, the nearest neighbors of a given voxel (i.e., 26 + 1 (including itself)) are uniformly covered in the grid h with the points $x_{ijk} = (x_i^1, x_j^2, x_k^3) = h(i,j,k)$ for $i,j,k = 1,2...M$, where M is the number of points on the grid in each spatial direction (for simplicity, we take the number of points on the grid equal in all directions). Depending on the type of region, at each point on the grid, we assign the interpolation of the updated metric tensors $\bar{m}_{ij}(x)$ or $\bar{g}_{ij}(x,y)$.

The flow chart in Fig. 5 summarizes the fiber tracking algorithm for HOT where ROI refers to the region of interest. ROI can avoid the processing of irrelevant image points and speed up the processing, where we have defined our stopping criteria, as mentioned in the algorithm below. Fig. 8 illustrates that our Finsler tractography approach can indeed resolve the crossings. Fibers are well recovered even when the Ricci noise level is 0.09 as shown in Fig. 9. However, we observe that if the noise is too high and the angle between the fibers is small, then some of the fibers result in kissing instead of crossing. The algorithm has the following steps:

1. Calculate the coefficients of the inverted diffusion profile (using fanDTasia ToolBox Barmpoutis et al. (2009); Barmpoutis and Vemuri (2010)) by inverting the signal data (see Section 5.1).
2. Set all voxels with $\mathrm{FA}_m(x) \geq 0.7$ as the initial position of the seed voxel with the principal directions corresponding to $\tilde{m}_{ij}(x)$, and set the flag value to 1 for these voxels.
3. Pick one of the seed voxels as the current position and mark its flag value zero.
4. For the current position voxel, make a cell of $3\times3\times3$ of the neighboring voxels $26+1$ and compute the updated metric tensors for them. Perform the trilinear interpolation on the finer grid that covers these voxels with $M = 9$ (for 2D, make a cell of 3×3 for the neighboring voxels of $8+1$ and compute accordingly).
5. Compute numerically the derivatives and Christoffel symbols, as defined in equations (8) and (13), respectively.
6. Feed the current position and direction to the RK4 method (ODE solver) and get the new refined position and direction of the fiber after a fixed number of steps. Next, remember the refined final position and the new voxel to which it belongs, and analyze the type of this new voxel position (see Fig. 5).

7. In the non-intersecting case, keeping the same refined position, replace the direction with the corresponding principal direction of $\tilde{m}_{ij}(x)$. In the intersecting case, choose the optimal direction-dependent metric and the gradient direction of the corresponding direction-dependent metric (see Fig. 5).
8. Repeat steps 4-7 until one of the stopping criteria is fulfilled, i.e., the new voxel position outside the domain, $FA_m(x) \leq 0.2$ (to avoid the isotropic region), the current voxel position does not change after a fixed iteration number (depending on the ODE solver step), if the starting position is the same as the ending position (to avoid an infinite loop) and stop after the maximum number of iterations (to prevent any other option of an infinite loop).
9. Save the detected fiber and set the flag value to 0 for all voxels touched by the detected path. Pick up a new seed voxel (if such a voxel still exists) by checking the flag values and repeat steps 3-8.
10. The saved fibers are the output of the procedure.

5.3. Segmetation using Tractography

In essence, medical image analysis involves image segmentation as the fundamental process to analyze the structure. The active contour model Kass, Witkin and Terzopoulos (1988) is also called the snake method commonly used for segmentation and is based on energy minimization. It is a biased contour that shrinks towards the object. This method requires user interaction and knowledge of the desired contour shape. It fails in many circumstances; e.g., for a simple donut shape in 2D, it either does not find the whole, or it shrinks up to one voxel and disappears (see Fig. 10 (a)).

Diverse image modalities can be employed to segment images into separate regions Mumford and Shah (1989); Malladi et al. (1995); Caselles et al. (1997); Sethian (1999); Chan and Vese (2001). In Chan and Vese (2001), they used a region-based energy model based on the formulation of Mumford and Shah (1989). The method was based on the minimization of global energy. This solved the problem with edge-based methods, but did not segment objects whose parts have non-homogeneous structures. For example, if the image contains objects that are brighter than the background and some that are darker than the background, the Chan and Vese (2001) method typically segments only bright or dark objects.

The problem mentioned above was addressed in Lankton and Tannenbaum (2008), using a localized curve model. They argued that the efficiency of the method depends on the choice of the similarity measure on the tensor. They used the Log-Euclidean metric and advocated improvement under this better similarity measure Lankton and Tannenbaum (2008).

In this work, we are resolving the limitations in Kaushik and Slovák (2018, 2019); Kaushik (2020). In particular, we implement the method directly in 3D and, moreover, initiating the segmentation by the localized fibers inside the object. We also eliminate the prospective failure when segmenting complex images such as closed loops (see Figs. 10 (a) and 11 (a)). We use second-order projections of 4th order tensors in our Finsler setting. The 2nd order tensor fields are obtained from $\tilde{m}_{ij}(x)$ available at a given position, which are SPD matrices and lie in Riemannian space (see equation (15)). The results show that this projection effectively reveals the geometry of the higher-order tensors.

To find the distance measure for the 2nd order tensor, we follow the spectral approach, which is based on treating the eigenvalues and eigenvectors of an SPD matrix separately. We use SQ interpolation for distance approximations, which is best suited even in the presence of noise Tschumperle and Deriche (2001). Geometrically, those SPD matrices form the cone $\mathbb{S}^+_n$ in $\mathbb{R}^{n^2}$, a manifold that contains an intrinsic Riemannian metric, here $n = 3$. If we restrict the group that acts on $\mathbb{S}^+$ to the special orthogonal group $SO(3)$, then the transposition of the matrix coincides with the inverse, and we can write the 2nd order tensor as $r = v\Lambda v^T$. Here, Λ is a diagonal matrix that contains all the eigenvalues of r, while v is an orthogonal matrix. Thus, we may consider the tensors in $\mathbb{S}^+$ as couples (v, Λ).

Considering two fixed tensors $r_1 = (v_1, \Lambda_1)$ and $r_2 = (v_2, \Lambda_2)$ we are interested in the relevant interpolation curve that joins them. This curve is a geodesic on the Lie group $G = SO(3) \times \mathbb{D}^+(3)$ with its natural metric, where $\mathbb{D}^+(3)$ is the group of diagonal matrices with positive elements. This Lie group is a 4:1 covering of $\mathbb{S}^+(3)$. The preimages of r are given by four different orientations, originating from rotation, by angle π around the principal axes of the ellipsoid associated with SPD r (including the trivial one). Let V be the preimage of $v_2 \in SO(3)$ then the distance between the two rotations v_1 and v_2 is defined as

$$dist(v_1, v_2) = \arg\min_{v \in V} dist(v_1, v_2) = \arg\min_{v \in V} \|log(v_1 v_2^T)\|_2, \tag{17}$$

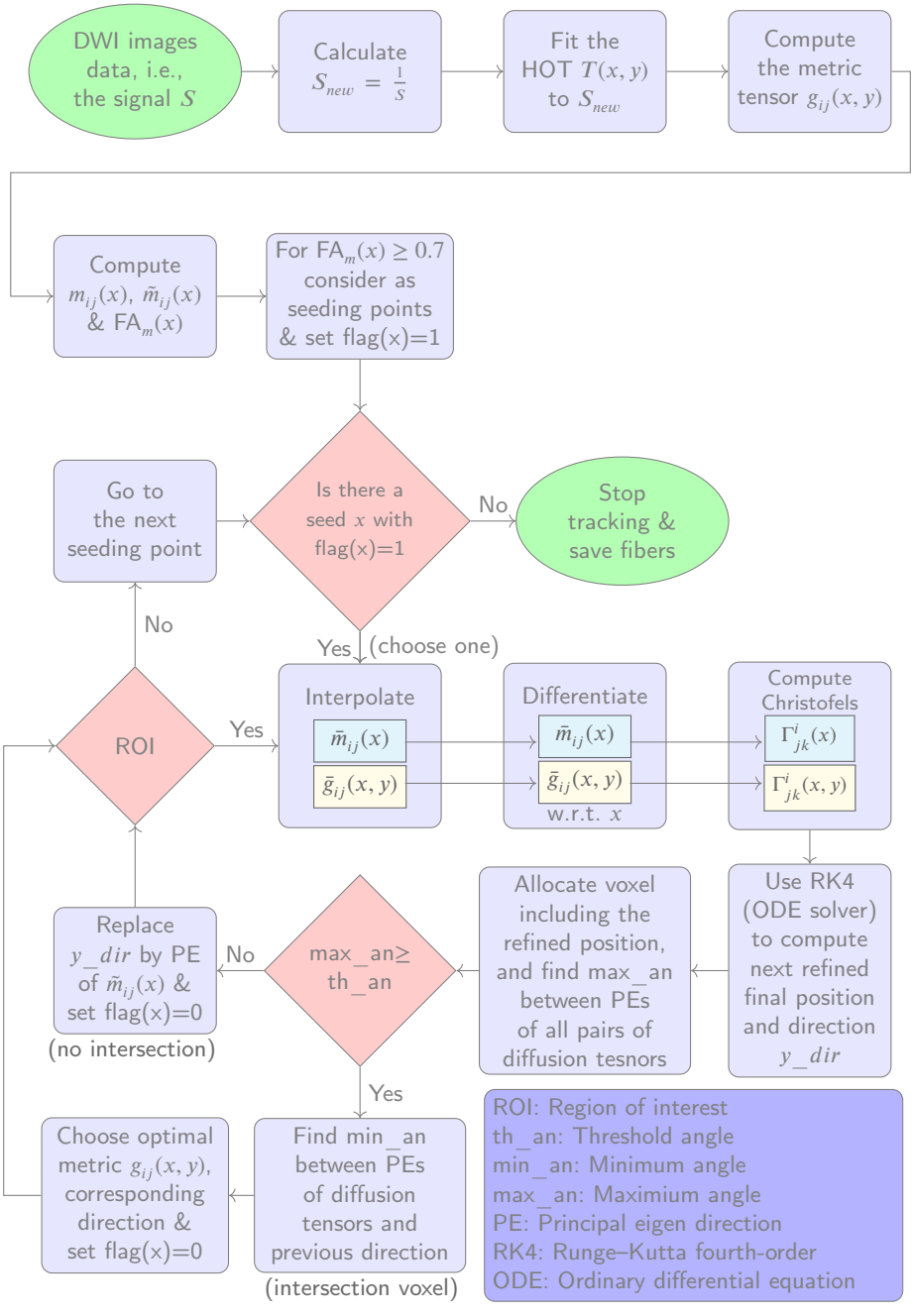

Fig. 5: Flow chart for fiber tracking in the Finsler space

and the interpolation curve is

$$r(t) = v(t)\Lambda(t)v(t)^T, \tag{18}$$

where $v(t) = v_1 \exp(t \log(v_1^T v_2))$ and $\Lambda(t) = \exp(1-t)\log(\Lambda_1) + t\log(\Lambda_2)$. For a more detailed discussion and formulation of the SQ metric, see Kaushik (2020).

We use the unbiased contour approach, which can shrink or expand depending on the image features. Our algorithm works automatically without user interaction. To avoid the choice of shape or size of the contour, we directly feed

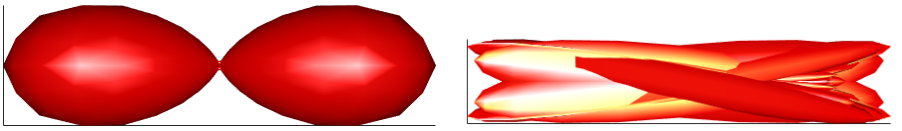

(a) Tensor (HOT) (b) 2nd order metric tensors

Fig. 6: a) Shows glyph of a 4th order tensor and b) depicts the first thirty tensors out of w, with the highest maximal eigenvalues.

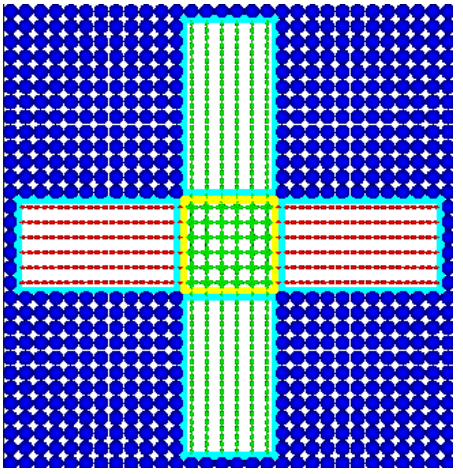

Fig. 7: In rectangular boxes, the cyan color shows one fiber is present per voxel. The yellow color shows two fibers present per voxel that indicate an intersection region. In our tractography method, for non-intersecting regions, we use the hybrid streamline Bihonegn et al. (2021) approach and in the case of intersection, we follow the optimal metric under Finslerian framework.

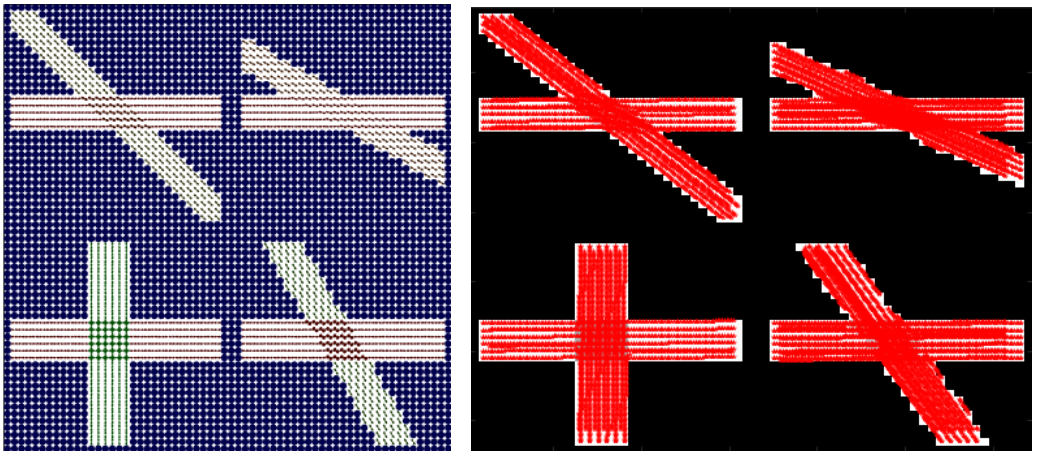

(a) Tensorial field (b) Tracography

Fig. 8: Tractography (without noise) for HARDI where the angle between the crossing fibers are 90°, 60°, 45° and 30°.

the detected fibers to initiate the contour. It can easily deal with much more complex shapes, such as crossings and closed-loop structures.

Fig. 10 clearly illustrates our claim in comparison with the approach in Kaushik and Slovák (2019). We show that the initial position of the contour plays a significant role in accurate segmentation. A better position of the contour reduces the number of iterations and reduces the overall time. Fig. 10 b) shows the segmentation using tractography

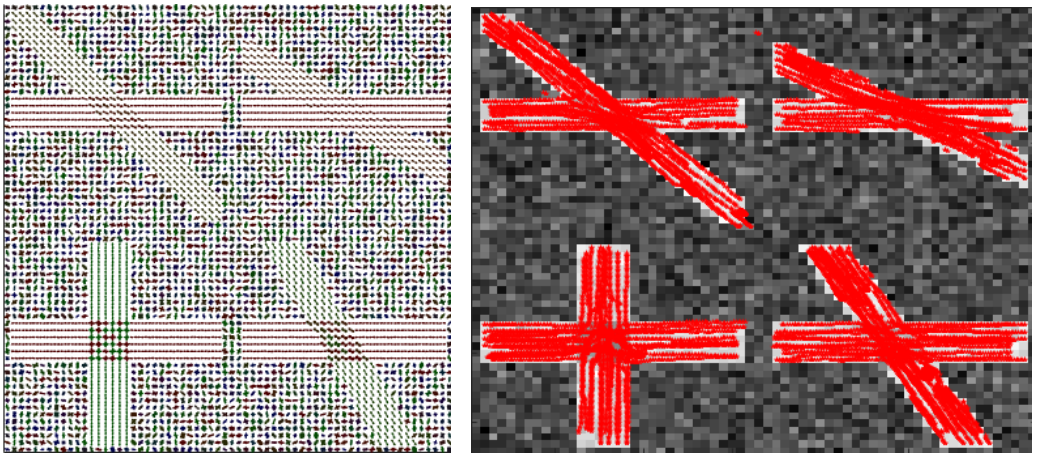

(a) Tensorial field (b) Tracography

Fig. 9: Tractography result with Ricci noise level 0.09 for Fig 8.

and takes less time to segment the image accurately. We show the fibers in red, and the magenta color represents the final segmented image. Fig. 10 c) shows an incomplete result where the segmentation fails. The contour in Fig. 10 d) is squeezed up to one voxel and shows that there is not even a partial result of segmentation. Figs. 10 e) and f) show that it fails to segment even after reaching the maximum iteration (i.e., 1000 iterations), indicating that the result will be the same after the saturation limit.

Fig. 11 a) shows the simulated tensorial field of the closed-loop structure in a more complex environment. Here, the choice of contour shapes like rectangles, circles, etc. will not work at all. Fig. 11 b) illustrates the segmented image (shown in magenta color) of the same tensorial field using tractography. After the fibers have been obtained, segmentation can be performed in very few iterations. Fig. 12 shows the segmentation flow chart using fiber tracking. The present study combines Finsler tractography approach with active contours to segment anisotropic structures in white matter regions.

5.4. Results on 3D Images

In our experiments, we also focus on results related to synthetic and real three-dimensional images. Fig. 13 illustrates how tractography and segmentation work. Fig. 13 a) shows a simulated tensor field obtained by combinations of three linear fibers that cross orthogonally, b) shows the tractography in red fibers on the corresponding scalar image, and c) illustrates the corresponding segmented image. Fig. 14 represents the performance of the proposed Finsler approach for tractography and segmentation in the central part of the brain. Fig. 15 illustrates the tractography results of Fig. 14 (a) viewed from different angles.

6. Conclusion and Future Scope

Inverting the higher-order tensor is a time-consuming and complex procedure. Proper inversion of HOT is required to preserve certain inversion properties. We introduced a novel way to invert the HOT in a straightforward way; this provides better information on the data. It preserves all inversion properties and helps us to track fibers in a better way. Additionally, we find that even in the case of HOT, sharpening of the inverse diffusion tensor can be achieved by powering the signal $S(\mathcal{g})$. However, in the current setting, our experiments are producing very satisfactory results without any sharpening.

Next, we resolved some shortcomings of the existing tractography in the Finslerian framework. We employ fiber tracking in the Finsler setting, which helps us to deal with complex fiber structures easily and works better for high-curvature and small-angle intersections between fibers, even in the presence of noise.

Finally, in view of the fact that the initial position of the contour plays a vital role, and in some complex images, the choice of contour shape (e.g., rectangle and circle) will not work at all. We segmented the brain images using fibers

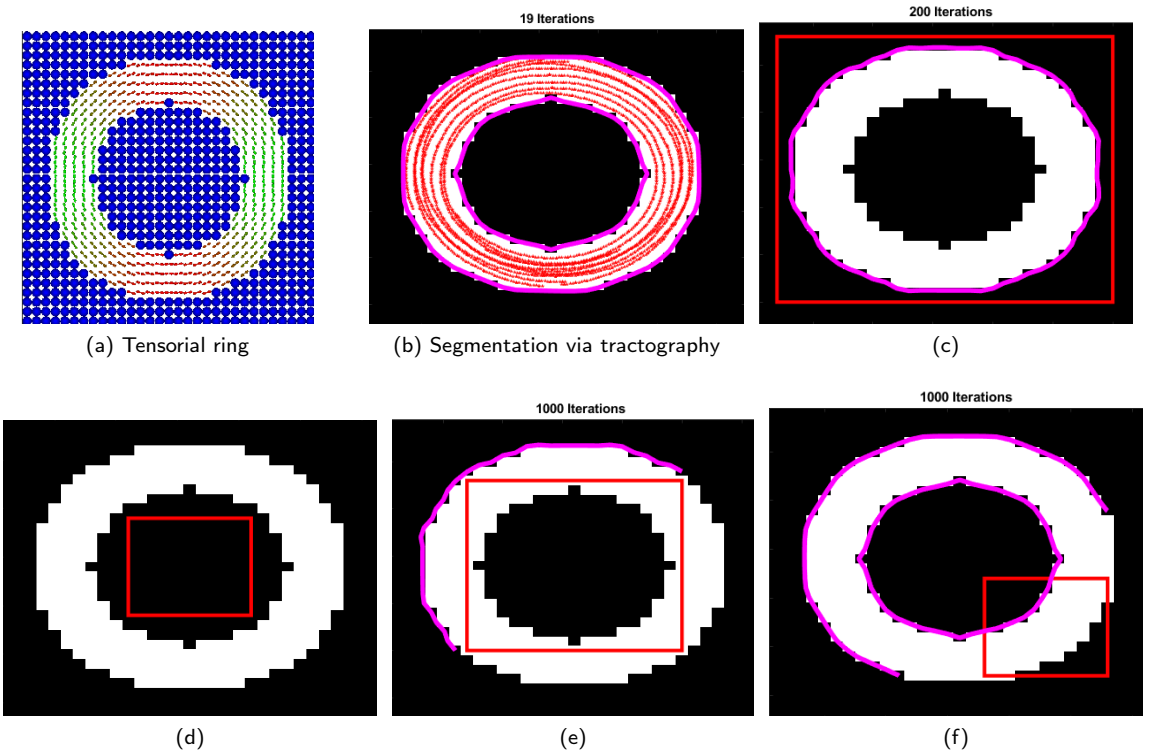

(a) Tensorial ring (b) Segmentation via tractography (c)

(d) (e) (f)

Fig. 10: a) Represents the tensorial field and b) illustrates the segmented image via tractography (fibers in red color). The rest of all sub-figures show the segmented images using the same approach in Kaushik and Slovák (2019) having the initial contour position as red rectangular boxes. Sub-figures c), d), e) and f) completely fail to segment at all. The magenta color shows the final segmented image. The maximum number of iterations is indicated at the top of the image.

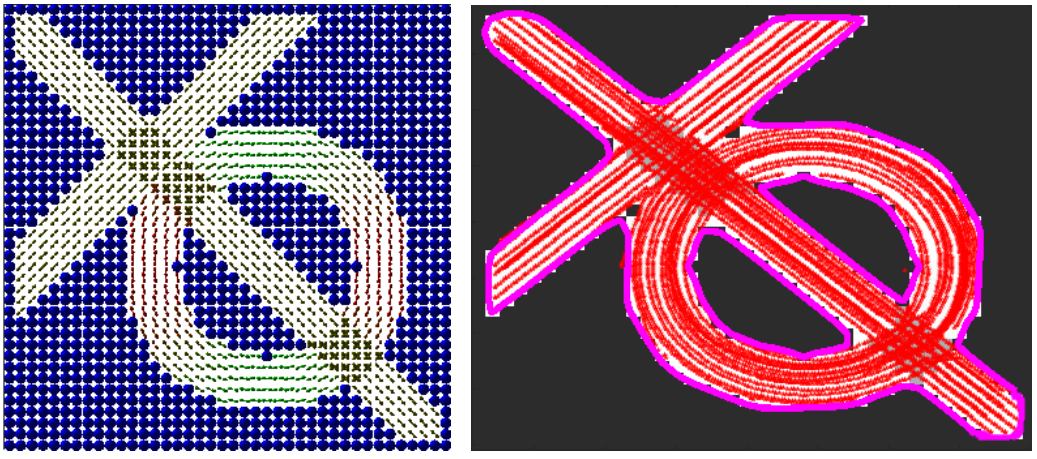

(a) Complex tensorial field (b) Segmentation via tractography

Fig. 11: a) Represents the tensorial field and b) illustrates the segmented image using tractography where red color represent fibers and the magenta color shows segmentation.

obtained from tractography as the initial contour. This method gives more flexibility to deal with complex structures accurately and faster without human interaction.

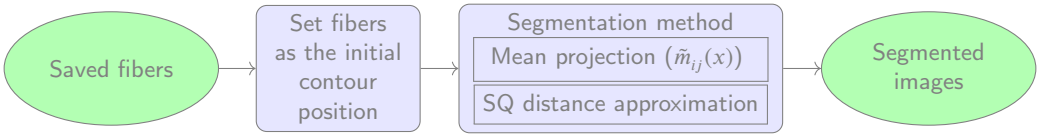

Fig. 12: Flow chart for segmentation

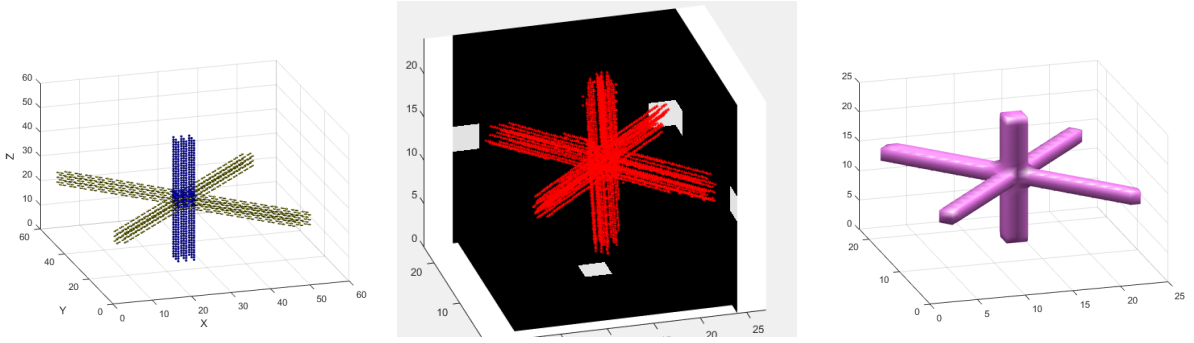

(a) Tensorial field (b) Tractography result on scalar image (c) Segmented image

Fig. 13: Tractography and segmentation result on the simulated tensorial field.

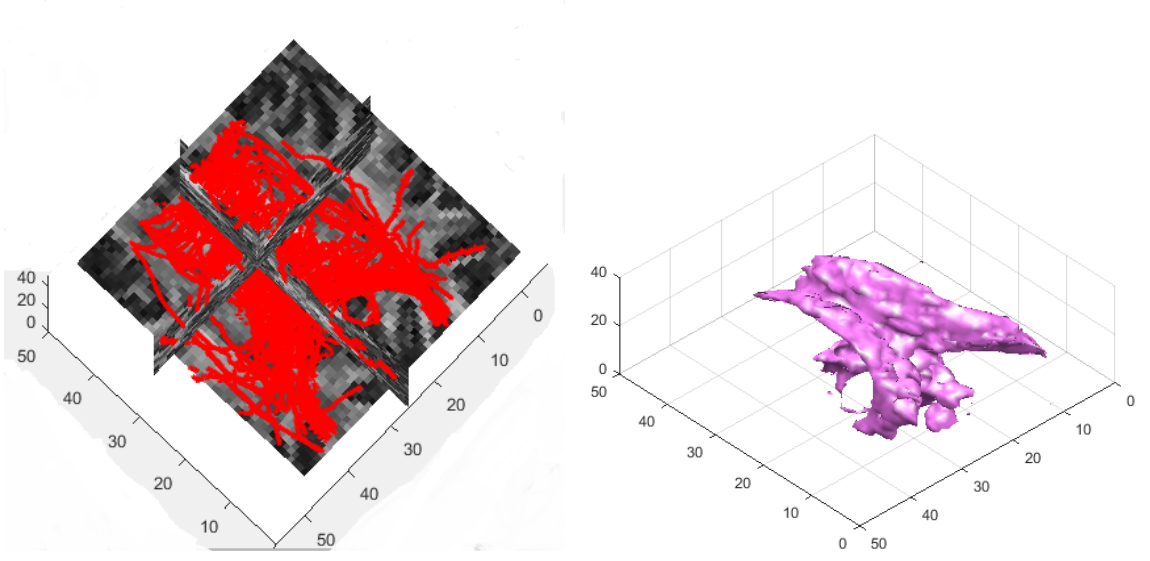

(a) Tractography (b) Segmented image

Fig. 14: Tractography and segmentation result on the real brain image.

The drawback of the proposed approach is that storing all direction-dependent metrics per voxel requires large memory and, due to high computation, is a very time-consuming process. In the future, we will focus on using features of the Finsler curvature to solve large-memory and computing challenges that can improve their effectiveness and efficiency.

Acknowledgements

The first author is supported by the MUNI/A/1092/2022 grant. The second author acknowledges support from the Research Council of Norway under the FRIPRO Researcher Project 302624. The third author acknowledges the support

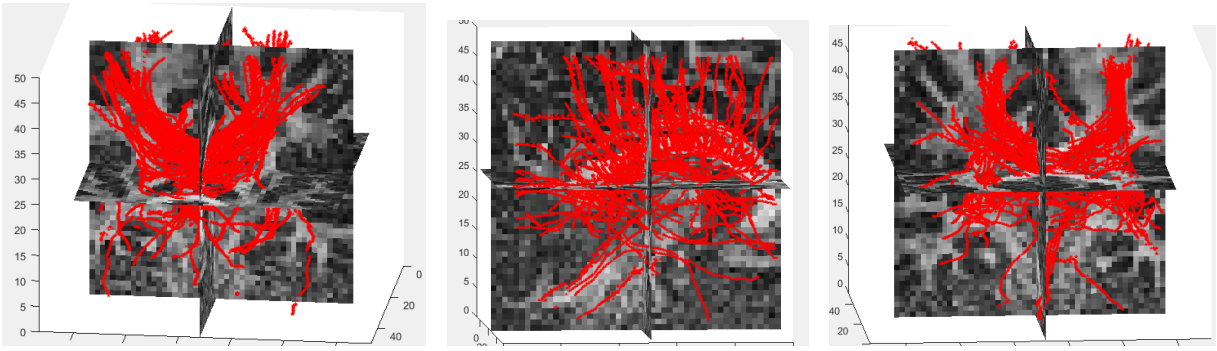

(a) (b) (c)

Fig. 15: The tractography result of Fig. 14 (a) viewed from different angles.

from the Operational Program Research, Development, and Education "Project Internal Grant Agency of Masaryk University No.CZ.02.2.69 /0.0/0.0/19-073/0016943". The first and last authors are also supported by the GA20-11473S grant from GACR.

Author Contributions

Avinash Bansal is the main author of this work. He prepared the manuscript, implemented the algorithms, and performed the experiments. Jan Slovak encouraged Avinash Bansal to investigate the diffusion HOT inversion profile and the Finsler tractography and supervised the findings of this work. Sumit Kaushik and Jan Slovak guided Avinash Bansal to segment using tractography. The proposed tractography algorithm is an enhancement of the work of Temesgen Bihonegn. All authors discussed the results and implications and edited the manuscripts at all stages of the work.

Conflicts of Interest

The Authors declare no conflicts of interest.

References

Astola, L., Florack, L., 2011. Finsler geometry on higher order tensor fields and applications to high angular resolution diffusion imaging. International Journal of Computer Vision 92, 325–336. URL: https://doi.org/10.1007/s11263-010-0377-z.

Astola, L., Jalba, A., Balmashnova, E., Florack, L., 2011. Finsler streamline tracking with single tensor orientation distribution function for high angular resolution diffusion imaging. Journal of Mathematical Imaging and Vision 41, 170–181. URL: https://doi.org/10.1007/s10851-011-0264-4.

Astola, L., Sepasian, N., Haije, T.D., Fuster, A., Florack, L., 2014. A simplified algorithm for inverting higher order diffusion tensors. Axioms 3, 369–379. URL: https://doi.org/10.3390/axioms3040369.

Bansal, A., Kaushik, S., Bihonegn, T., Slovák, J., 2021. Geodesic ray-tracing in white matter fiber crossing region using decomposition of 4th order tensor, in: Rittner, L., M.D., E.R.C., Lepore, N., Brieva, J., Linguraru, M.G. (Eds.), 17th International Symposium on Medical Information Processing and Analysis, International Society for Optics and Photonics. SPIE. pp. 228 – 235. URL: https://doi.org/10.1117/12.2606129.

Barmpoutis, A., Hwang, M.S., Howland, D., Forder, J.R., Vemuri, B.C., 2009. Regularized positive-definite fourth order tensor field estimation from dw-mri. NeuroImage 45, S153–S162. URL: https://doi.org/10.1016/j.neuroimage.2008.10.056.

Barmpoutis, A., Vemuri, B.C., 2010. A unified framework for estimating diffusion tensors of any order with symmetric positive-definite constraints, in: 2010 IEEE international symposium on biomedical imaging: from nano to macro, IEEE. pp. 1385–1388. doi:10.1109/ISBI.2010.5490256.

Basser, P.J., Mattiello, J., LeBihan, D., 1994a. Estimation of the effective self-diffusion tensor from the NMR spin echo. Journal of Magnetic Resonance, Series B 103, 247–254. URL: https://doi.org/10.1006/jmrb.1994.1037.

Basser, P.J., Mattiello, J., LeBihan, D., 1994b. Mr diffusion tensor spectroscopy and imaging. Biophysical journal 66, 259–267. URL: https://doi.org/10.1016/S0006-3495(94)80775-1.

Basser, P.J., Pajevic, S., Pierpaoli, C., Duda, J., Aldroubi, A., 2000. In vivo fiber tractography using dt-mri data. Magnetic resonance in medicine 44, 625–632. URL: https://doi.org/10.1002/1522-2594(200010)44:4<625::AID-MRM17>3.0.CO;2-O.

Behrens, T.E., Woolrich, M.W., Jenkinson, M., Johansen-Berg, H., Nunes, R.G., Clare, S., Matthews, P.M., Brady, J.M., Smith, S.M., 2003. Characterization and propagation of uncertainty in diffusion-weighted mr imaging. Magnetic Resonance in Medicine: An Official Journal of the International Society for Magnetic Resonance in Medicine 50, 1077–1088. URL: https://doi.org/10.1002/mrm.10609.

Bihonegn, T., Kaushik, S., Bansal, A., Vojtíšek, L., Slovák, J., 2021. Geodesic fiber tracking in white matter using activation function. Computer Methods and Programs in Biomedicine 208, 106283. URL: https://doi.org/10.1016/j.cmpb.2021.106283.

Björnemo, M., Brun, A., Kikinis, R., Westin, C.F., 2002. Regularized stochastic white matter tractography using diffusion tensor mri, in: International Conference on Medical Image Computing and Computer-Assisted Intervention, Springer. pp. 435–442. URL: https://doi.org/10.1007/3-540-45786-0_54.

Brannon, R.M., 2018. Rotation, Reflection, and Frame Changes. 2053-2563, IOP Publishing. doi:10.1088/978-0-7503-1454-1.

Caselles, V., Kimmel, R., Sapiro, G., 1997. Geodesic active contours. Int. J. Comput. Vision 22, 61–79. URL: https://doi.org/10.1023/A:1007979827043.

Chan, T.F., Vese, L.A., 2001. Active contours without edges. IEEE Transactions on image processing 10, 266–277. doi:10.1109/83.902291.

Chu, C.Y., Huang, J.P., Sun, C.Y., Zhang, Y.L., Liu, W.Y., Zhu, Y.M., 2015. Multifiber pathway reconstruction using bundle constrained streamline. Computerized Medical Imaging and Graphics 46, 291–299. doi:https://doi.org/10.1016/j.compmedimag.2015.07.010.

de Luis-García, R., Westin, C.F., Alberola-López, C., 2011. Gaussian mixtures on tensor fields for segmentation: Applications to medical imaging. Computerized Medical Imaging and Graphics 35, 16–30. doi:https://doi.org/10.1016/j.compmedimag.2010.09.001.

Dela Haije, T., Sepasian, N., Fuster, A., Florack, L., 2016. Adaptive enhancement in diffusion mri through propagator sharpening, in: Computational Diffusion MRI. Springer, pp. 131–143. URL: https://doi.org/10.1007/978-3-319-28588-7_12.

Descoteaux, M., Deriche, R., 2009. High angular resolution diffusion mri segmentation using region-based statistical surface evolution. Journal of Mathematical Imaging and Vision 33, 239–252. URL: https://doi.org/10.1007/s10851-008-0071-8.

Descoteaux, M., Lenglet, C., Deriche, R., 2007. Diffusion tensor sharpening improves white matter tractography, in: Medical Imaging 2007: Image Processing, SPIE. pp. 531–539. URL: https://doi.org/10.1117/12.708988.

Do Carmo, M.P., Flaherty Francis, J., 1992. Riemannian geometry. volume 6. Springer.

Fletcher, P.T., 2013. Geodesic regression and the theory of least squares on riemannian manifolds. International journal of computer vision 105, 171–185. URL: https://doi.org/10.1007/s11263-012-0591-y.

Fletcher, P.T., Lu, C., Joshi, S., 2003. Statistics of shape via principal geodesic analysis on lie groups, in: 2003 IEEE Computer Society Conference on Computer Vision and Pattern Recognition, 2003. Proceedings., IEEE. pp. I–I. doi:10.1109/CVPR.2003.1211342.

Friman, O., Farneback, G., Westin, C.F., 2006. A bayesian approach for stochastic white matter tractography. IEEE transactions on medical imaging 25, 965–978. doi:10.1109/TMI.2006.877093.

Fuster, A., et al., 2016. Adjugate diffusion tensors for geodesic tractography in white matter. Journal of Mathematical Imaging and Vision 54, 1–14. URL: https://doi.org/10.1007/s10851-015-0586-8.

Ghosh, A., Papadopoulo, T., Deriche, R., 2012. Biomarkers for HARDI: 2nd & 4th order tensor invariants, in: 2012 9th IEEE International Symposium on Biomedical Imaging (ISBI), IEEE. pp. 26–29. doi:10.1109/ISBI.2012.6235475.

Gur, Y., Johnson, C.R., 2014. Generalized HARDI invariants by method of tensor contraction, in: 2014 IEEE 11th international symposium on biomedical imaging (ISBI), IEEE. pp. 718–721. doi:10.1109/ISBI.2014.6867971.

Hagmann, P., Jonasson, L., Deffieux, T., Meuli, R., Thiran, J.P., Wedeen, V.J., 2006. Fibertract segmentation in position orientation space from high angular resolution diffusion mri. NeuroImage 32, 665–675. URL: https://doi.org/10.1016/j.neuroimage.2006.02.043.

Hao, X., Whitaker, R.T., Fletcher, P.T., 2011. Adaptive riemannian metrics for improved geodesic tracking of white matter, in: Biennial International Conference on Information Processing in Medical Imaging, Springer. pp. 13–24. URL: https://doi.org/10.1007/978-3-642-22092-0_2.

Kass, M., Witkin, A., Terzopoulos, D., 1988. Snakes: Active contour models. International journal of computer vision 1, 321–331. URL: https://doi.org/10.1007/BF00133570.

Kaushik, S., 2020. Geometric Approach to Segmentation in Diffusion Magnetic Resonance Imaging [online]. Doctoral theses, dissertations. Masaryk University, Faculty of Science, Brno. URL: https://is.muni.cz/th/thsvd/. supervisor: Jan Slovák.

Kaushik, S., Slovák, J., 2018. Dti segmentation using anisotropy preserving quaternion based distance measure, in: International Conference Image Analysis and Recognition, Springer. pp. 81–89. URL: https://doi.org/10.1007/978-3-319-93000-8_10.

Kaushik, S., Slovák, J., 2019. Hardi segmentation via fourth-order tensors and anisotropy preserving similarity measures. Journal of Mathematical Imaging and Vision 61, 1221–1234. URL: https://doi.org/10.1007/s10851-019-00897-w.

Kingsley, P.B., 2006. Introduction to diffusion tensor imaging mathematics: Part i. tensors, rotations, and eigenvectors. Concepts in Magnetic Resonance Part A 28, 101–122. URL: https://doi.org/10.1002/cmr.a.20048.

Krajsek, K., Menzel, M.I., Scharr, H., 2016. A riemannian bayesian framework for estimating diffusion tensor images. International Journal of Computer Vision 120, 272–299. URL: https://doi.org/10.1007/s11263-016-0909-2.

Lankton, S., Tannenbaum, A., 2008. Localizing region-based active contours. IEEE transactions on image processing 17, 2029–2039. doi:10.1109/TIP.2008.2004611.

Lenglet, C., Rousson, M., Deriche, R., Faugeras, O., Lehericy, S., Ugurbil, K., 2005. A riemannian approach to diffusion tensor images segmentation, in: Biennial International Conference on Information Processing in Medical Imaging, Springer. pp. 591–602. URL: https://doi.org/10.1007/11505730_49.

Liu, C., Mang, S.C., Moseley, M.E., 2010. In vivo generalized diffusion tensor imaging (gdti) using higher-order tensors (hot). Magnetic Resonance in Medicine: An Official Journal of the International Society for Magnetic Resonance in Medicine 63, 243–252. URL: https://doi.org/10.1002/mrm.22192.

Malladi, R., Sethian, J., Vemuri, B., 1995. Shape modeling with front propagation: a level set approach. IEEE Transactions on Pattern Analysis and Machine Intelligence 17, 158–175. doi:10.1109/34.368173.

Melonakos, J., Pichon, E., Angenent, S., Tannenbaum, A., 2008. Finsler active contours. IEEE Transactions on Pattern Analysis and Machine Intelligence 30, 412–423. doi:10.1109/TPAMI.2007.70713.

Mori, S., Crain, B.J., Chacko, V.P., Van Zijl, P.C., 1999. Three-dimensional tracking of axonal projections in the brain by magnetic resonance imaging. Annals of Neurology: Official Journal of the American Neurological Association and the Child Neurology Society 45, 265–269. URL: https://doi.org/10.1002/1531-8249(199902)45:2<265::AID-ANA21>3.0.CO;2-3.

Mumford, D.B., Shah, J., 1989. Optimal approximations by piecewise smooth functions and associated variational problems. Communications on pure and applied mathematics doi:10.1002/cpa.3160420503.

Özarslan, E., Shepherd, T.M., Vemuri, B.C., Blackband, S.J., Mareci, T.H., 2006. Resolution of complex tissue microarchitecture using the diffusion orientation transform (dot). NeuroImage 31, 1086–1103. doi:10.1016/j.neuroimage.2006.01.024.

O'Donnell, L., Haker, S., Westin, C.F., 2002. New approaches to estimation of white matter connectivity in diffusion tensor mri: Elliptic pdes and geodesics in a tensor-warped space, in: International Conference on Medical Image Computing and Computer-Assisted Intervention, Springer. pp. 459–466. URL: https://doi.org/10.1007/3-540-45786-0_57.

Pennec, X., Fillard, P., Ayache, N., 2006. A riemannian framework for tensor computing. International Journal of computer vision 66, 41–66. URL: https://doi.org/10.1007/s11263-005-3222-z.

Prakash, K., Zhou, S., Morgan, T.C., Hanley, D.F., Nowinski, W.L., 2012. Segmentation and quantification of intra-ventricular/cerebral hemorrhage in ct scans by modified distance regularized level set evolution technique. International journal of computer assisted radiology and surgery 7, 785–798. doi:10.1007/s11548-012-0670-0.

Schultz, T., Fuster, A., Ghosh, A., Deriche, R., Florack, L., Lim, L.H., 2014. Higher-order tensors in diffusion imaging, in: Visualization and Processing of Tensors and Higher Order Descriptors for Multi-Valued Data. Springer, pp. 129–161. URL: https://doi.org/10.1007/978-3-642-54301-2_6.

Sepasian, N., ten Thije Boonkkamp, J.H., Florack, L.M., Romeny, B.M.T.H., Vilanova, A., 2014. Riemann-finsler multi-valued geodesic tractography for hardi, in: Visualization and Processing of Tensors and Higher Order Descriptors for Multi-Valued Data. Springer, pp. 209–225. URL: https://doi.org/10.1007/978-3-642-54301-2_9.

Sethian, J.A., 1999. Level set methods and fast marching methods: evolving interfaces in computational geometry, fluid mechanics, computer vision, and materials science. volume 3. Cambridge university press.

Shen, Z., 2001. Lectures on Finsler geometry. World Scientific.

Tournier, J.D., Calamante, F., Gadian, D.G., Connelly, A., 2004. Direct estimation of the fiber orientation density function from diffusion-weighted mri data using spherical deconvolution. Neuroimage 23, 1176–1185. URL: https://doi.org/10.1016/j.neuroimage.2004.07.037.

Tournier, J.D., Yeh, C.H., Calamante, F., Cho, K.H., Connelly, A., Lin, C.P., 2008. Resolving crossing fibres using constrained spherical deconvolution: validation using diffusion-weighted imaging phantom data. Neuroimage 42, 617–625. URL: https://doi.org/10.1016/j.neuroimage.2008.05.002.

Tschumperle, D., Deriche, R., 2001. Diffusion tensor regularization with constraints preservation, in: Proceedings of the 2001 IEEE Computer Society Conference on Computer Vision and Pattern Recognition. CVPR 2001, IEEE. pp. I–I. doi:10.1109/CVPR.2001.990631.

Tuch, D.S., et al., 2002. Diffusion MRI of complex tissue structure. Ph.D. thesis. Massachusetts Institute of Technology. URL: http://hdl.handle.net/1721.1/8348.

Vuorinen, M., 2006. Conformal geometry and quasiregular mappings. volume 1319. Springer.

Wang, Y., Zhao, Y., Guo, Z., Qi, M., Fan, Y., Meng, H., 2019. Diffusion tensor image segmentation based on multi-atlas active shape model. Multimedia Tools and Applications 78, 34231–34246. URL: https://doi.org/10.1007/s11042-019-08051-9.